Thermoelectric optimization of AgBiSe_{2} by defect engineering for room-temperature applications

Zhenzhen Feng, Xiaoli Zhang, Yuanxu Wang, Jihua Zhang, Tiantian Jia, Bingqiang Cao, and Yongsheng Zhang

Phys. Rev. B **99**, 155203 — Published 17 April 2019

DOI: 10.1103/PhysRevB.99.155203

Thermoelectric optimization of $AgBiSe_2$ for room temperature applications by defect engineering

Zhenzhen Feng[1,2], Xiaoli Zhang[1,2], Yuanxu Wang[3], Jihua Zhang[4], Tiantian Jia[1,2], Bingqiang Cao[5] and Yongsheng Zhang[1,2,*]

[1]Key Laboratory of Materials Physics, Institute of Solid State Physics, Chinese Academy of Sciences, Hefei 230031, China

[2]Science Island Branch of the Graduate School, University of Science and Technology of China, Hefei 230026, China

[3]Institute for Computational Materials Science, School of Physics and Electronics, Henan University, Kaifeng 475004, China

[4]Guizhou Provincial Key Laboratory of Computational Nano-Material Science, Guizhou Education University, Guiyang 550018, China

[5]School of Physics and Physical Engineering, Shandong Provincial Key Laboratory of Laser Polarization and Information Technology, Qufu Normal University, Qufu 273165, China

E-mail: yshzhang@theory.issp.ac.cn

Abstract:

The hexagonal phase of $AgBiSe_2$ has been discovered as a promising thermoelectric material for the room temperature applications. However, its basic conduction type is still ambiguous and its current ZT value is pretty low. To improve the thermoelectric performance of $AgBiSe_2$, we apply the band engineering to modify its band structure by introducing defects to increase the band degeneracy. From the calculated intrinsic point defect formation energies of $AgBiSe_2$ at different growth conditions, we clarify that the conducting behavior of $AgBiSe_2$ is a *p*-type semiconductor, and the Ag vacancy is the dominated acceptor. Based on scrutinizing the band structure of $AgBiSe_2$, two kinds of methodologies can be used to modify its band structure to achieve high band degeneracy: (1) shifting the Fermi level into the valence band using intrinsic defects and (2) converging several valence band maxima by introducing extrinsic defects. We find that the intrinsic Ag vacancy is helpful to significantly increase the power factor, leading to a large ZT for Ag vacancy-doped $AgBiSe_2$: the maximum ZT value is increased to 0.3-0.5 at near room temperature. Based on analyzing the bonding characters and atomic energy levels in the compound,

we predict several extrinsic dopants (Cu, Rh and Pd) that can be used to converge three valence band maxima. Our work provides methodologies to improve the room temperature thermoelectric applications of $AgBiSe_2$ by tuning its band structures using intrinsic or extrinsic defects.

I. Introduction

Thermoelectric materials enable direct conversion between thermal and electrical energy, and offer a promising solution for harvesting waste heat to useful electrical power. Thermoelectric performance is quantified by the figure of merit, $ZT = S^2\sigma T/(\kappa_e+\kappa_l)$, where S, σ, T, κ_e, and κ_l are the Seebeck coefficient, the electrical conductivity, the absolute temperature, the electrical and lattice components of thermal conductivity κ, respectively [1]. Because of the complex interdependence of S, σ, and κ, it is an extreme challenge to enhance the ZT value. Recently, two major strategies have been adopted to improve the thermoelectric performance. One is to increase the electrical properties through engineering the band structure to achieve large band degeneracy [2,3] or to form localized resonant states [4]. The other one is to reduce the lattice thermal conductivity (κ_l, an independent thermoelectric parameter) by forming a solid solution [5,6], searching compounds with the strong lattice anharmonicity [7-11] or liquid-like atomic behavior [12].

It is important to reiterate that the electrical transport properties is dominated by the details of the band structure and scattering mechanism. The optimized electrical transport properties of a thermoelectric material depends on the weighted mobility [2,13], $\mu(m^*_{DOS}/m_e)^{3/2}$, where m^*_{DOS} and m_e are the density of states (DOS) effective mass and the electron mass, respectively. The DOS effective mass is given [13,14]: $m^*_{DOS} = N_V^{2/3} m^*_b$, where N_V is the band degeneracy and m^*_b is the band effective mass. For the charge carries predominantly scattered by acoustic phonons, the mobility can be given as: $\mu \propto 1/{m^*_b}^{5/2}$. Therefore, decreasing the band effective mass will increase the carrier mobility. To result in the large Seebeck coefficient without detriment the mobility, the high band degeneracy (N_V) is requested to produce large m^*_{DOS}. Thus, an effective way to improve the electrical transport performance is to reconstruct the band structure near the Fermi level to increase N_V, such as shifting the Fermi level into the band structure or aligning several bands maxima will active the multiple bands and enhanced S and the power factor ($PF = S^2\sigma$). This is the so-called band structure engineering [15]. The extrinsic Mg doping in SnTe [16] can shrink the energy difference between the light- and heavy-hole valence band maxima of SnTe, which remarkably enhances its power factor. For the effect of intrinsic defects, theoretical calculations conclude that Ag_{Mg} antisite defects significantly increase the

thermoelectric performance of α-MgAgSb by increasing the number of band valleys near the Fermi level [17]. Therefore, engineering the band structure by introducing intrinsic or extrinsic point defects, is an effective strategy to improve the thermoelectric properties in a lot of thermoelectric materials [18].

Using the band structure engineering, many high thermoelectric performance materials have been identified, such as half-Heusler [6], Zintl compounds [19], $CoSb_3$ skutterudites [3], and so on. However, these compounds have the maximum ZT value at a relatively high temperature (for example, the n-type skutterudite material with a ZT value of 1.3 at 850 K [20]), which are suitable for the medium- and high-temperature applications. Thermoelectric applications at low temperature (especially at room temperature) lead to a huge business opportunity, such as harvesting energy using heat from living beings. However, few materials are suitable for the low temperature applications. Although Bi_2Te_3-based alloys with a ZT value of unity have been using as the only thermoelectric materials for the room-temperature device since 1950 [21,22], the scarcity and high cost of Te element limit their commercially widespread applications. It is meaningful to seek alternative high performance thermoelectric materials at low temperature (300-550 K) with constitute elements relatively cheap and abundantly available in the earth's crust. Recently, the hexagonal phase of $AgBiSe_2$ has been attracted increasing attention for the room temperature applications. Obviously, compared to Te in Bi_2Te_3, Ag in $AgBiSe_2$ is more available and have large mass abundance in the Earth's crust [23].

$AgBiSe_2$ crystallizes in a hexagonal structure at room temperature. It undergoes two structural phase transitions [24-29] at a higher temperature, ~460 K (hexagonal to rhombohedral) and ~580 K (rhombohedral to cubic). $AgBiSe_2$ has the intrinsic low lattice thermal conductivity (0.45 W/mK at 300 K [30,31]). Enhancing the power factor of the compound is thus the essential way to improve its thermoelectric performance at room temperature. However, the conducting behavior of $AgBiSe_2$ is not clear, which hinders its thermoelectric property tuning using carrier concentrations. Xiao *et al*. reported that the room-temperature hexagonal $AgBiSe_2$ phase is an intrinsic *p*-type semiconductor [30,31]. Parker *et al*. demonstrated that the good room-temperature *p*-type thermoelectric properties might attribute to its one-dimensional "plate-like" carrier pocket anisotropy in the valence band [23]. However, Pan *et al*. suggested that such a phase is an intrinsic *n*-type semiconductor instead of *p*-type, and they claimed that the

different conductive types may due to contamination or unintentional doping during the experiment [32]. Due to lacking results about carrier concentration, it is difficult to give a rational explanation of the differences [32]. It is known that defects play important roles in the properties of semiconductors, such as the carrier conduction and corresponding thermoelectric properties. Hence, it is imperative to clarify the conduction type of the room temperature $AgBiSe_2$ phase and optimize its thermoelectric properties through the band structure engineering.

In this work, for the room-temperature hexagonal $AgBiSe_2$ phase, we calculate the defect formation energies of different intrinsic charged point defects at different chemical potentials, and find that the formation energies strongly depend on the chemical potential. Under the Ag rich condition, Ag vacancy is the dominated intrinsic defects, and the Ag vacancy defect is more stable than other intrinsic defects under the Se rich condition. Thus, the acceptor defects (Ag vacancy) lead the *p*-type conduction behavior of $AgBiSe_2$. By studying the band structure of $AgBiSe_2$, we find that the valence bands exhibit multiple valleys, and the energy differences between the valence band maximum (VBM), the secondary and tertiary valence bands are small. This band feature implies that the electrical transport properties could be improved by the band structure engineering. Two methodologies introducing intrinsic and extrinsic defects are used to tune its band structure. The most stable intrinsic Ag vacancy defects can directly shift the Fermi level into the valence band. Alternatively, analyzing the bonding characters in $AgBiSe_2$, we find that the number of band degeneracy can be largely increased by tuning the position of Ag-*d* orbital. From the calculated atomic energy levels of different atoms, we predict that the thermoelectric properties of $AgBiSe_2$ can be improved by introducing Cu, Rh, and Pd. Therefore, our work sheds light on improving the room-temperature thermoelectric performance of $AgBiSe_2$ by introducing the intrinsic and extrinsic point defects.

II. Method

A. Density functional theory calculations

The structures of pristine room temperature $AgBiSe_2$ (hexagonal) phase and the corresponding compounds with intrinsic and extrinsic defects are optimized utilizing the plane-wave projector augmented-wave (PAW) method [33] using the Vienna ab

initio simulation package (VASP) [34] based on density functional theory (DFT). The generalized gradient approximation (GGA) of Perdew−Burke−Ernzerhof (PBE) [35] is used as the exchange-correlation functional. The energy cutoff for plane wave expansion is 500 eV. The lattice constants of the hexagonal $AgBiSe_2$ phase are a=b=4.19 Å, c=19.87 Å, containing 12 atoms. To simulate various defects in the hexagonal $AgBiSe_2$ cell, we use a (3 × 3 × 1) supercell containing 108 atoms to largely eliminate the periodic image interactions. A (3 × 3 × 2) Γ-centered Monkhorst-Pack k-point grid was employed to sample the Brillouin zone (BZ) of the supercell.

The semi-local exchange correlation potential (such as GGA-PBE) suffers from the well-known band gap underestimation. To correct the band gap to achieve reliable electrical properties, we adopt the Tran and Blaha modified semi-local Becke–Johnson exchange correlation potential (TB-mBJ) [36]. The corresponding electronic structures of $AgBiSe_2$ are calculated using the full-potential linearized augmented plane wave method [37], as implemented in WIEN2k [38,39]. The muffin-tin radii (R_{MT}) were set to 2.5 a.u. for Ag, Bi, and Se. The cut-off parameter $R_{mt} \times K_{max} = 9$ (K_{max} is the magnitude of the largest k vector) is used, and the self-consistent calculations are performed with the (9 × 9 × 2) k-mesh in the irreducible Brillouin zone for $AgBiSe_2$. Taking 10000 k-points in the Brillouin zone, we calculate the electrical transport properties using the semiclassical Boltzmann transport theory (BTE) [40,41] within the constant scattering time approximation as implemented in the Boltz-TraP code [42]. To shift the Fermi level the right position and investigate the influence of Ag vacancy defects on the electronic structure and thermoelectric properties, we use a (4 × 4 × 1) supercell (196 atoms in the $AgBiSe_2$ supercell) corresponding to a doping level of 2%. The self-consistent calculations are performed with a (2 × 2 × 2) k-mesh in the irreducible Brillouin zone. Since the supercell calculation has the well-known band folding in the BZ, we unfold the band structure of the supercell using the band unfolding technique, developed by Popescu and Zunger [43].

B. Defect formation energy calculations

We consider three types of intrinsic point defects (vacancy, interstitial, and antisite defects) in $AgBiSe_2$. The cation/anion antisites always have high formation energies [44,45] due to their large differences in atomic radius, these cation/anion antisites (such as Ag or Bi on the Se site, and Se on the Ag or Bi sites) are not discussed in current work. The following intrinsic defects are denoted as V_{Ag} (Ag vacancy), V_{Bi} (Bi vacancy), V_{Se} (Se vacancy), Ag_I (Ag interstitial), Bi_I (Bi interstitial), Se_I (Se interstitial), Ag_{Bi} (Ag on the Bi site), and Bi_{Ag} (Bi on the Ag site). The defect formation enthalpies (ΔH_f) are calculated using the following formula,

$$\Delta H_{D,q}(E_F, \mu) = E_{D,q} - E_H + \sum_i n_i\mu_i + q(E_F + E_V + \Delta V) + E_{corr}, \quad (1)$$

where $E_{D,q}$ and E_H are the total energies of supercells with and without defects, respectively. The integer n_i represents the number of type *i* atom that have been added to ($n_i > 0$) or removed from ($n_i < 0$) the supercell. The chemical potentials μ_i are expressed relative to the reference elemental phase such that $\mu_i = \mu_i^0 + \Delta\mu_i$, where μ_i^0 is the chemical potential of the elemental solid and $\Delta\mu_i$ is the change of the chemical potential between the defect system and the elemental solid. E_F is the Fermi energy, E_V is the energy with respect to the valence band maximum (VBM), and ΔV is the averaged difference between the local potential far from the defect in the defective supercell and the corresponding one in the perfect supercell. E_{corr} is the image charge corrections in a charged supercell, and we use the Lany and Zunger correction method [46].

III. Results and Discussion

A. Chemical potentials and formation energies of intrinsic point defect

Introducing defects in a compound is an effective way to tune its band structure and possibly improve its thermoelectric performance. Appling Eq. 1 to calculate the defect formation energy in $AgBiSe_2$, we should firstly determine the chemical potential

of each element. Due to the complex phase transitions and the appearance of secondary phases, previous experimental works suggested that it is difficult to synthesize pure hexagonal phase of $AgBiSe_2$ [24]. However, carefully controlling the chemical potential during experimental synthesis may solve the problem. The chemical potentials of constituent species can be varied to reflect specific equilibrium growth conditions, and they are globally constrained by the formation enthalpy of the host to maintain its stability. Thus for $AgBiSe_2$, we can write as,

$$\mu_{AgBiSe_2} = \mu_{Ag} + \mu_{Bi} + 2\mu_{Se}, \quad (2)$$

$$E_{AgBiSe_2} = E_{Ag} + E_{Bi} + 2E_{Se} + \Delta H(AgBiSe_2), \quad (3)$$

where $\mu_{AgBiSe2}$ and μ_X are the chemical potentials of $AgBiSe_2$ and an element X (Ag, Bi, or Se), respectively. E_X is the energy of solid X. ΔH is the heat formation energy of a compound in the unit of eV per formula unit. Under the equilibrium condition for the crystal growth, $\mu_{AgBiSe_2} = E_{AgBiSe_2}$, which means:

$$\Delta H(AgBiSe_2) = \Delta\mu_{Ag} + \Delta\mu_{Bi} + 2\,\Delta\mu_{Se}, \quad (4)$$

where $\Delta\mu_X = \mu_X - E_X$. For $AgBiSe_2$, our calculated heat formation energy ΔH is -1.1 eV/f.u.. At the X-rich condition, $\mu_X = E_X$ and $\Delta\mu_X = 0$. Thus, to avoid the elemental bulk precipitation (Ag or Bi or Se), the upper limits of their chemical potential should set as

$$\Delta\mu_{Ag} \le 0, \ \Delta\mu_{Bi} \le 0, \ \Delta\mu_{Se} \le 0. \quad (5)$$

Additionally, to avoid forming any competing phases (such as Ag_2Se, $BiSe_2$, Bi_2Se_3, Bi_3Se_4, and Bi_4Se_3) during the $AgBiSe_2$ growth, the chemical potential $\Delta\mu_{Ag}$, $\Delta\mu_{Bi}$, and $\Delta\mu_{Se}$ must further satisfy the following limits:

$$2\Delta\mu_{Ag} + \Delta\mu_{Se} \le \Delta H(Ag_2Se), \ \Delta\mu_{Bi} + 2\Delta\mu_{Se} \le \Delta H(BiSe_2),$$

$$2\Delta\mu_{Bi} + 3\Delta\mu_{Se} \le \Delta H(Bi_2Se_3), \ 3\Delta\mu_{Bi} + 4\Delta\mu_{Se} \le \Delta H(Bi_3Se_4),$$

$$4\Delta\mu_{Bi} + 3\Delta\mu_{Se} \le \Delta H(Bi_4Se_3). \quad (6)$$

These constraints (Eq. 4-6) enclose an accessible area of chemical potentials ($\Delta\mu_{Ag}$,

$\Delta\mu_{Bi}$) for forming the thermodynamically stable $AgBiSe_2$ compound, and the available stable range is illustrated as the red shaded region in Fig. 1 (The vertices of this stable region are labeled as A, B, C, D, and E). From the chemical potentials of elements at A-E (Table I), we notice that the points (A and C) and (B and D) refer to the Ag-rich ($\Delta\mu_{Ag}$= 0) and Se-rich ($\Delta\mu_{Se}$= 0) conditions, respectively. Additionally, the coordinate of point E is ($\Delta\mu_{Ag}$, $\Delta\mu_{Bi}$, $\Delta\mu_{Se}$) = (-0.2, -0.48, -0.21) eV. Thus, the intrinsic defect formation energies in $AgBiSe_2$ are calculated based on these chemical potentials.

From the formation energies of intrinsic point defects (V_{Ag}, V_{Bi}, V_{Se}, Ag_I, Bi_I, Se_I, Ag_{Bi}, Bi_{Ag}) in their neutral charge states as a function of chemical potential (Fig. 2), for the two experimentally suggested defects (the Ag vacancy V_{Ag} and the Ag_{Bi} antisite defect) [30,31], we find that V_{Ag} has the lowest formation energy, which is much lower than that of Ag_{Bi}. This indicates that it is V_{Ag} not Ag_{Bi} can be easily formed in $AgBiSe_2$, which is inconsistent with the previously experimentally observed Ag vacancies defects in $AgBiSe_2$ [47]. The experimental results suggest that the two kinds of defects can be actually coexisted in the $AgBiSe_2$ growth. Owing to the importance of charged defects in semiconductors, it is worth to consider the influence of the point charge on the defect formation energy. Then, we calculated the formation energy of the charged defects ($V_{Ag}^{0/-1}$, $V_{Bi}^{0/-1/-2/-3}$, $V_{Se}^{0/+1/+2}$, $Ag_I^{0/+1}$, $Bi_I^{0/+1/+2/+3}$, $Se_I^{0/-1/-2}$, $Ag_{Bi}^{0/-1/-2}$, $Bi_{Ag}^{0/+1/+2}$). According to Eq. 1, the formation energy of a charged defect depends on the Fermi energy level E_F, which is varying within the band gap. Our theoretically calculated band gap of the pristine $AgBiSe_2$ is 0.69 eV, which is in good agreement with the experimentally measured value (~0.6 eV) [24]. We here take the experimentally measure ~0.6 eV to constrain the E_F region (using the theoretically calculated 0.69 eV does not affect our conclusions). The Fermi levels at the valence band maximum (VBM) and the conduction band minimum (CBM) in our formation energy calculations are set to 0.0 and 0.6 eV, respectively. We calculate the formation energies of the charged intrinsic point defects in the hexagonal $AgBiSe_2$ phase (Fig. 3) at the three conditions: the Ag-rich [point-B in Fig. 1, ($\Delta\mu_{Ag}$, $\Delta\mu_{Bi}$, $\Delta\mu_{Se}$) = (0, -0.68, -0.21) eV], Se-rich [point-B in Fig. 1, ($\Delta\mu_{Ag}$, $\Delta\mu_{Bi}$, $\Delta\mu_{Se}$) = (-0.11, -0.99, 0) eV] and (c) Ag-rich/more Se-poor [point-C in Fig. 1, ($\Delta\mu_{Ag}$, $\Delta\mu_{Bi}$, $\Delta\mu_{Se}$) = (0, -0.12 eV, -0.49 eV)] conditions. The chemical potentials in the formation energy calculations are close to the experimental synthesis environment. From Eq. (1) and our calculated formation energies, we can see

that the formation energies of the intrinsic point defects strongly depend on the chemical potentials.

It is expected that removal of a cation or adding an extra electron in the antisite defect will result in a net electron deficiency and generate unoccupied acceptor levels [44]. Such empty defect levels are called shallow acceptor levels if situated slightly above the VBM. This helps to produce positive holes (*p*-type carriers) in the valence band, giving rise to the *p*-type conductivity. Under the Ag rich (point-A in Fig. 1) condition (Fig. 3-a) and the Ag rich/more Se-poor (point-C in Fig. 1) condition (Fig. 3-c), the formation energy of the Ag vacancy defects is low, meaning that they can be easily formed in $AgBiSe_2$ and are the dominant acceptors. Thus, in the *p*-type conductivity, it can be realized by forming the Ag vacancy defects, which is consistent with the results reported by Xiao *et al*. [30,31]. Under the Se-rich (point-B in Fig. 1) condition (Fig. 3-b), the Ag vacancy defect has the lowest defect formation energy (the black line in Fig. 3-b), which is obvious that the Ag vacancy is preferred in the Ag-poor environment. However, under both Ag-rich and Se-rich conditions, the formation energy of the defects with a net hole [such as the Se vacancy (V_{Se}), interstitial (Ag_I, Bi_I) and Bi_{Ag} antisite defects] are pretty high, indicating that those defects are hardly formed under the two conditions and the *n*-type conductivity is not preferred. On the basis of the formation energies in the defect diagram (Fig. 2 and Fig. 3), we clarify that the low temperature hexagonal $AgBiSe_2$ phase is an intrinsic p-type semiconductor. The defect influenced thermoelectric properties can be carried out in the followings.

B. Electronic band structure of $AgBiSe_2$

The hexagonal $AgBiSe_2$ phase is stable at T < ~460 K, and the compound is suggested as a room-temperature thermoelectric material. Owing to the low lattice thermal conductivity of $AgBiSe_2$ at room temperature, enhancing the electrical properties (such as the power factor, PF) of the compound is an important strategy to achieve the high thermoelectric performance. The electrical properties of a compound strongly depend on its electronic structure or band structure. As we mentioned before, introducing intrinsic or extrinsic defects is an effective methodology to tune the band structure and optimize the electrical transport properties. From our theoretically calculated band structure (Fig. 4-a) using the MBJ band gap correction method, $AgBiSe_2$ is a semiconductor with an indirect band gap of 0.69 eV, the VBM locating

between the K and Γ points and the CBM at the A point in the BZ. The theoretical band gap value is in good agreement with the experimentally measured 0.6 eV [24], which is reasonably consistent with the previously theoretically calculated 0.52 eV [23]. The difference between the theoretical calculated band gap is due to Ref. [23] just relaxed the internal coordinates of the $AgBiSe_2$ pristine structure.

It is known that a large band degeneracy N_V is beneficial to a large DOS effective mass m^*_{DOS} without deterioration of the carrier mobility μ [2]. N_V is based on the effective total number of independent carrier pockets or valleys in the Brillouin zone, including both symmetry and orbital degeneracies. For PbTe [2], the compound has the light hole bands at the VBM. After heavy hole doping, its Fermi level shifts down into the valence band, allowing a high band degeneracy and a large amount of holes from the secondary and tertiary valence band.

From our theoretically calculated $AgBiSe_2$ band structure (Fig. 4-a), we notice that the secondary and tertiary valence band maxima locate at L-H (VB_2) and Γ-M (VB_3), which are just 0.05 and 0.1 eV lower than that of the VBM, respectively. The small energy difference between the three valence band maxima indicates that the $AgBiSe_2$ compound would show a high converged band at valence band maximum. Such a good band features associate with the high thermoelectric properties [17]. Thus, we could shift the Fermi level to those secondary and tertiary valence band maxima to increase the band degeneracy N_V by doping. If the bands of all these maxima are degenerated or the Fermi level crosses all these maxima at the same time, the power factor of the compound will be significantly enhanced. From the theoretically calculated isoenergy surfaces near the VBM (Fig. 4-b-d), with lowing the Fermi level to -0.01 eV (VBM-0.01), -0.06 eV (VBM-0.06) and -0.11 eV (VBM-0.11), the number of band degeneracy N_V is increasing from 6 to 12, and 18, respectively. Finally, in the case of -0.11 eV (VBM-0.11, slightly below VB3), we notice that there are 6 pockets along K-Γ, 24 quarter-pockets along L-H, and 6 pockets along Γ-M. Therefore, the isoenergy surface of the energy level at around the maximum of VB3 (VBM-0.1) has a high degeneracy with 18 isolated pockets. However, for the isoenergy surface of the conduction bands, CBM+0.01eV corresponding to the Fermi energy across the energy of +0.01eV (Fig. S1 in Supplementary Material [48]) has 2 half-pockets at X point, i.e. the full number of the valley is 1. Moreover, the anisotropic band edge of a pocket is favorable for the thermoelectric performance [49,50]. The isoenergy surfaces of the CBM pockets are

close to ellipsoids, whereas the VBM ones are deviations from the ellipsoidal or spherical shapes. The high degeneracy (large N_V) and the anisotropic isoenergy surface of the valence band are beneficial to the high power factor [51]. Thus, we expect that the *p*-type $AgBiSe_2$ has a better power factor than the *n*-type one.

C. Effect of intrinsic defects on band structures and electrical properties

Once the Fermi level reaches the VB3 maximum (Fig. 4-a), it will generate a high pocket degeneracy of 18 and 0.028 holes in the cell (the corresponding carrier concentration is about 2.8×10^{20} cm^{-3} at 300 K). Accurately controlling heavy doping can move the Fermi level to the right position. Under the Ag-rich and Se-rich conditions, since the Ag vacancy (V_{Ag} in Fig. 3) defect has the lowest formation energy, we focus on how the intrinsic Ag vacancy defect optimize the electrical transport properties.

To calculate the defect influenced band structures, we build a ($4 \times 4 \times 1$) supercell with 192 atoms ($Ag_{48}Bi_{48}Se_{96}$) and remove one Ag from the supercell to form a V_{Ag} ($Ag_{47}Bi_{48}Se_{96}$, 2% of Ag vacancy). Using the MBJ potential, the band structures of $Ag_{47}Bi_{48}Se_{96}$ and the corresponding non-defect $Ag_{48}Bi_{48}Se_{96}$ for comparison are given in Supplementary Materials [48], Fig. S2-a and -b, and the corresponding unfolded band structures of the two supercells are shown in Fig. 5. As seen from Fig. 5(b) and Fig. S2-b, the most obvious change in the band structure with introducing the intrinsic V_{Ag} defect is the Fermi level shifting into the valence bands, which shows the typical *p*-type behavior. In addition, the number of band degeneracy (N_V) near the Fermi level is increased. This leads to two main advantages: (1) The large band degeneracy contributes to the possible high Seebeck coefficient; (2) Since the carrier concentration depends on the number of band valleys near the Fermi level, a high carrier concentration will help to increase the electrical conductivity. Therefore, *p*-type $AgBiSe_2$ with the intrinsic V_{Ag} defects will play an important role in achieving high electrical transport properties.

We then solve the BTE to calculate the thermoelectric properties (Fig. 6) of the pristine $AgBiSe_2$ and V_{Ag} systems as a function of temperature at three different carrier concentrations (10^{19}, 10^{20}, 10^{21} holes/cm^3). Since the BTE calculated electrical conductivity σ/τ includes the hardly defined carrier scattering relaxation time τ, we are going to use the experimentally measured electrical conductivity data from Ref. [25] to obtain its value. The relaxation time (τ) takes into account the contributions from both

acoustic and optical phonons. From the standard electron-phonon interactions (for both acoustic and optical phonons) [52-54], τ decreases with increasing temperatures, showing the T^{-1} behavior. Additionally, the relaxation time has a relationship with the carrier concentration (n) as $n^{-1/3}$. Thus, the relaxation time τ can be written as, $\tau=C_0T^{-1}n^{-1/3}$, where C_0 is the constant number required to be determined. We then calculate the electrical conductivity σ/τ of the pristine and V_{Ag} $AgBiSe_2$ systems using the BTE. By matching these calculated results with the experimentally measured electrical conductivities [25] of the corresponding systems at the same carrier concentration and temperature, we can obtain the constant number C_0. Since we focus on the thermoelectric properties at the low temperature region, we choose the calculated and experimental data at [300 K, 1.96×10^{20} cm^{-3}] and [300 K, 0.93×10^{20} cm^{-3}] for $AgBiSe_2$ and V_{Ag}, respectively. This leads C_0 as 5.3×10^{-7} and 4.3×10^{-6} (sK/cm) for the pristine and V_{Ag} $AgBiSe_2$ systems, respectively. These constant numbers can thus be used as the simple approach to evaluate the relaxation time at different temperature and concentrations as $\tau= 5.3\times10^{-7}$ $T^{-}n^{-1/3}$ and $\tau= 4.3\times10^{-6}$ $T^{-}n^{-1/3}$ for the pristine and V_{Ag} $AgBiSe_2$ systems, respectively, with the unit of τ in s, T in K, and n in cm^{-3}. Moreover, in order to verify the electron relaxation time, taking the pristine $AgBiSe_2$ compound as an example, we calculate its τ using the deformation potential approach (Fig. S3 in Supplemental Material [48]). It turns out that the electron relaxation times from the two methodologies (the experimental fitting and the deformation potential approach) are in reasonable agreement with each other, e.g. 8.2×10^{-16} s (exp.) vs 1.1×10^{-15} s (cal.) at the carrier concentration of 10^{19} cm^{-3} and 300 K. Moreover, the comparisons between the calculated temperature-dependent thermoelectric properties (*S*, σ, and ZT) of $AgBiSe_2$ and the other experimental measurements [47] are shown in Fig. S3. From Fig. S3, we can see that the experimentally measured results fall within the theoretical predicted regions considering different carrier concentrations. This can be considered reasonable agreement between the theoretical predictions and the experimental measurements. In the realistic applications, various dopants introducing electrons (or holes) are needed to manipulate the semiconductor as a p- (or n-) type. And we just consider the p-type doping for $AgBiSe_2$, the electrical transport properties were obtained at the carrier concentration in a range of 10^{19}-10^{21} cm^{-3}, which has been applied to many materials [55-58]. From the calculated electrical conductivities (Fig. 6-a) of the pristine and V_{Ag} defected systems, we find that σ of the V_{Ag} system is larger than that of pristine

$AgBiSe_2$.

The comparisons between the calculated temperature-dependent thermoelectric properties (*S*, σ, and ZT) of $AgBiSe_2$ and the experimental measurements are shown in Fig. S3. From Fig. S3, we can see that the experimentally measured results fall within the theoretical predicted regions considering different carrier concentrations. This can be considered reasonable agreement between the theoretical predictions and the experimental measurements. From the calculated electrical conductivities (Fig. 6-b) of the $AgBiSe_2$ and V_{Ag} defected systems, we find that σ of the V_{Ag} system is larger than that of $AgBiSe_2$.

For the Seebeck coefficient (*S*), it depends on the carrier concentration and temperature [59],

$$S = \frac{8\pi k_B^2}{3eh^2} N_V^{2/3} m_b^* T\left(\frac{\pi}{3n}\right)^{\frac{2}{3}}. \quad (7)$$

From the calculated Seebeck coefficient of the $AgBiSe_2$ and V_{Ag} defected systems, we notice that the *S* behavior can be explained using Eq. (7): it is proportional to temperature, yet is inversely related to the carrier concentration. Morever, we notice that *S* of the V_{Ag} defected system is smaller than that of the $AgBiSe_2$ compound, which is due to the increased carrier concentration. Without considering the large band degeneracy, *S* should be more strongly decreased. In other words, the band degeneracy maintains a suitable *S* with doping. The combination of high relaxation time and large band degeneracy in the V_{Ag} system will significantly increase the power factor and the corresponding ZT value. This confirms that the high band degeneracy in V_{Ag} suggests the increased power factor compared to the $AgBiSe_2$. The experimentally measured thermal conductivity is about 0.45 W/mK from room temperature to 500 K [30]. Bocher et al. [47] also reported that Ag vacancy defects in $AgBiSe_2$ have little effect (0.01 W/mK) on the thermal conductivity from room temperature to 500 K. Thus, it is reasonable to use a constant thermal conductivity value at the low temperature region to evaluate the ZT values of this two systems. Assuming that the thermal conductivity is a constant value, we could simulate the ZT value of this two systems. A significant enhancement of thermoelectric performance of the hexagonal $AgBiSe_2$ phase at the

low/mid-temperature region is realized through intrinsic Ag vacancy doping (Fig. 6-c): At the carrier concentration of 10^{19} holes/cm^3 between 200 and 460 K, introducing Ag vacancies increases the ZT values to 0.3-0.5. The large ZT value at room temperature is achieved by manipulating the $AgBiSe_2$ band structure through forming Ag vacancies. The ZT value is comparative to (or even larger than) that using the solid-solutioned homojunction nanoplates ($AgBi_{0.5}Sb_{0.5}Se_2$) [31], includeing Bi/Sb point defects and boundaries to scatter different wavelength phonons, decrease the thermal conductivity and increase the ZT value to 0.2 at room temperature. Therefore, introducing the intrinsic Ag vacancy by carefully controlling the $AgBiSe_2$ growth condition can significantly improve the thermoelectric performance of $AgBiSe_2$ for the room temperature applications.

D. Extrinsic defects tuning the band structure and electrical properties

We have investigated that the presence of intrinsic Ag vacancies in $AgBiSe_2$ shifts the Fermi level into the valence band resulting in high degenerated bands and heavy hole concentrations, which plays an essential role in the high power factor and possible high thermoelectric performance. Alternatively, we could converge or align the three valence bands (VBM, VB2 and VB3) by using extrinsic defects. To do so, we should firstly understand the contributions of atomic orbitals to the three valence bands. From the atom-projected density of states (PDOS, Fig. 7-a) of $AgBiSe_2$, we notice that the valence band (from VBM to -5.2 eV) are mainly dominated by the hybridization of Ag-*d* and Se-*p* orbitals. Based on the hybridizations between atomic orbitals (Fig. 7-a), we could roughly distinguish the bonding and antibonding regions of two orbitals: The bonding (-5.2~-3.5 eV) and antibonding (-2.5~0.0 eV) regions of Ag-*d* and Se-*p*, the bonding (-10.8~-9.0 eV) and antibonding (-1.0~0.0 eV) regions of Se-*p* and Bi-*s*, and the bonding (-5.2~-4.0 eV) and antibonding (CBM to 3.6 eV) regions of Bi-*p* and Se-*d*.

Based on the above discussion and the calculated relevant atomic energy level of the Ag, Bi, and Se atoms in Table II, we can obtain a schematic diagram of atomic

orbital interactions for $AgBiSe_2$ as shown in Fig. 7-b, where the bonding and antibonding states are formed in the shaded region. Then the positions of bonding and antibonding states match with the corresponding states in PDOS in Fig. 7-a. From the chemical bonding schematic view (Fig. 7-b), we can clearly see that the top valence band is mainly composed of the antibonding states of Se-*p* with Ag-*d* and of Se-*p* with Bi-*s*, and the bottom conduction band is mainly composed of the antibonding states of Se-*p* with Bi-*p*. Therefore, we can modify the valence band by tuning the Ag-*d*, Se-*p*, or Bi-*s* position. However, since tuning the Se-*p* orbital will affect the conduction band as well, this leaves the Ag-*d* or Bi-*s* orbitals to modify the valence band. Moreover, since the contribution of the Bi-*s* orbital on the top valence band is relatively small, the features of the valence band can be significantly adjusted by solo tuning the Ag-*d* orbital without affecting the conduction band.

From the projection of the band structure onto the Ag-*d* orbital (Fig. 8), we notice that VBM and VB2 have higher Ag-*d* components than VB3. This indicates that the modification of Ag-*d* orbital will mainly influence VBM and VB2 rather than VB3. If VBM and VB2 could shift downward to VB3, the number of band degeneracy will be obviously increased. As we are known, the weak interatomic interaction will shrink the gap between the bonding and antibonding states, i.e. pushing up the bonding states while drawing down the antibonding states. Since VBM and VB2 represent the antibonding of Se-*p* and Ag-*d* orbitals, they can be drawn down by decreasing their interactions. The *p*-*d* interactions can be decreased by increasing the on-site energy difference between the two orbitals. The current energy difference between Se-*p* and Ag-*d* orbitals is about 1.1 eV (Table II). We calculate the atomic energy levels of many elements (Fe/Co/Ni/Cu/Ru/Rh/Pd/Os/Ir/Pt/Au) with *d* orbital, and select four elements X (X=Cu, Rh, Ru and Pd in Table II) whose energy differences between X-*d* and Se-*p* are larger than 1.1 eV: 1.41, 2.9, 2.95, and 1.94 eV, for Cu, Ru, Rh and Pd, respectively. The larger energy difference between Se-*p* and X-*d*, the lower the antibonding states are. This is responsible for the three bands convergence. With an appropriate

Cu/Ru/Rh/Pd doping concentration in $AgBiSe_2$, the number of hole pockets will be enlarged.

We calculate the formation energies of Cu/Ru/Rh/Pd doping in $AgBiSe_2$. Beside the chemical potential constrains in the pristine $AgBiSe_2$ compound (Eq. 5, 6), additional constrains of chemical potentials for impurity doping should be used to avoid the formation of impurity-related phases. For Cu, Ru, Rh and Pd doping, the chemical potential of these elements are constrained by,

$$\Delta\mu_{Cu} \leq 0,\ 3\Delta\mu_{Cu} + 2\Delta\mu_{Se} \leq \Delta H(Cu_3Se_2),$$

$$\Delta\mu_{Cu} + \Delta\mu_{Se} \leq \Delta H(CuSe),\ \Delta\mu_{Cu} + 2\Delta\mu_{Se} \leq \Delta H(CuSe_2). \quad (8)$$

$$\Delta\mu_{Ru} \leq 0,\ \Delta\mu_{Ru} + 2\Delta\mu_{Se} \leq \Delta H(RuSe_2). \quad (9)$$

$$\Delta\mu_{Rh} \leq 0,\ 3\Delta\mu_{Rh} + 8\Delta\mu_{Se} \leq \Delta H(Rh_3Se_8),$$

$$\Delta\mu_{Rh} + \Delta\mu_{Se} \leq \Delta H(RhSe),\ \Delta\mu_{Rh} + 2\Delta\mu_{Se} \leq \Delta H(RhSe_2). \quad (10)$$

$$\Delta\mu_{Pd} \leq 0,\ 4\Delta\mu_{Pd} + \Delta\mu_{Se} \leq \Delta H(Pd_4Se),\ \Delta\mu_{Pd} + 2\Delta\mu_{Se} \leq \Delta H(PdSe_2),$$

$$7\Delta\mu_{Pd} + 2\Delta\mu_{Se} \leq \Delta H(Pd_7Se_2),\ 7\Delta\mu_{Pd} + 4\Delta\mu_{Se} \leq \Delta H(Pd_7Se_4). \quad (11)$$

At the Ag-rich [point-A (0, -0.68 eV, -0.21 eV) in Fig. 1], Se-rich [point-B (-0.11 eV, -0.99 eV, 0) in Fig. 1] and Ag-rich/Se-poor [point-C (0, -0.12 eV, -0.49 eV) in Fig. 1] conditions, these equations lead to the chemical potentials constrains of Cu, Ru, Rh and Pd (Table III). For example, at the Ag-rich [point-A (0, -0.68 eV, -0.21 eV) in Fig. 1] condition, these equations lead $\Delta\mu_{Cu} \leq$ -0.09 eV. So in this case, the $\Delta\mu_{Cu}$ = -0.09 eV is used for the calculation of formation energy for Cu-related defects.

The calculated formation energies of the Cu, Rh, Rh, Pd-doped $AgBiSe_2$ systems are shown in Fig. S5 (Supplemental Material [48]). For Cu- and Rh-doping at the Ag-rich/Se-poor condition (point-C in Fig. 1) condition, Cu and Rh tend to substitute the Ag atoms in $AgBiSe_2$ since Cu_{Ag} and Rh_{Ag} have the lower formation energy than other defects (Fig. S5 in Supplemental Material [48]). Pd is easier to occupy Ag site at the other Ag-rich (point-A in Fig. 1) condition. However, for Ru-doping, it is preferred to substitute Bi not Ag due to Ru_{Bi} has the lowest formation energy. Thus, Ru is hard to be doped at the Ag site.

In order to understand the effects of impurities on the electrical properties, we calculate band structures using a (2 × 2 × 1) $AgBiSe_2$ supercell (containing 48 atoms) with one impurity atom (Cu, Ru, Rh, or Pd, Fig. S6 in Supplementary Material [48]). From the band structures, the energy differences between the three valence band maxima become smaller for Cu, Rh, and Pd-doped $AgBiSe_2$ compared to the pristine compound, leading to the band convergence and the Seebeck coefficient (or power factor) enhancement. Moreover, Pd doping will induce the resonant states near the valence band, which usually lead to the improved Seebeck coefficient, as has been demonstrated in many thermoelectric materials [4,60,61]. Such band degeneracy and resonant states do not affect by the impurity concentration with a larger supercell calculations [one impurity atom in a (3 × 3 × 1) supercell containing 108 atoms, Fig. S7 in Supplementary Material [48]].Therefore, the valence band structure of $AgBiSe_2$ can be modified by extrinsic defects (Cu, Rh and Pd), and the increased band degeneracy and induced resonant states imply an improvement of power factor and the corresponding ZT value.

IV. Conclusions

We have systematically studied the intrinsic defect formation energies, the electronic structure and the thermoelectric performance of the $AgBiSe_2$ using density functional theory calculations. The conducting behavior of $AgBiSe_2$ is clarified as *p*-type and we find that the intrinsic Ag vacancy is the dominant defects, acting as the acceptors. The band structure engineering induced by intrinsic and extrinsic defects is a useful tool to achieve high thermoelectric properties. A high ZT value (0.3-0.5) of $AgBiSe_2$ can be achieved using the intrinsic defects (Ag vacancies) to increase the band degeneracy. Moreover, the enhancement of the valence band degeneracy is predicted by introducing extrinsic Cu/Rh/Pd dopants in $AgBiSe_2$, which indicates that these dopants can be used to improve the low-temperature ZT of $AgBiSe_2$. Our work not only suggests that *p*-type $AgBiSe_2$ is a promising room temperature thermoelectric material, but also provide methodologies to increase the band degeneracy by introducing intrinsic and extrinsic point defects.

Acknowledgments

The work was supported by the National Natural Science Foundation of China, Grants Nos. 11474283, 11774347 and 11547011. J. Z. acknowledges the NSF from science and technology department of Guizhou province (Nos. QKJC [2016]1113, QHPT [2017]5790-02). Z. Feng thanks the financial support from the China Scholarship Council (CSC). The calculations were performed in TianHe-2 at LvLiang Cloud Computing Center of China and at the Center for Computational Science of CASHIPS, the ScGrid of the Supercomputing Center, and the Computer Network Information Center of the Chinese Academy of Science. The authors are grateful for helpful discussion with Prof. David J. Singh and Dr. Yuhao Fu.

References

[1] X. Shi, L. Chen, and C. Uher, Int. Mater. Rev. **6**, 1 (2016).

[2] Y. Pei, X. Shi, A. LaLonde, H. Wang, L. Chen, and G. J. Snyder, Nature **473**, 66 (2011).

[3] Y. Tang, Z. M. Gibbs, L. A. Agapito, G. Li, H. S. Kim, M. B. Nardelli, S. Curtarolo, and G. J. Snyder, Nat. Mater. **14**, 1223 (2015).

[4] J. P. Heremans, V. Jovovic, E. S. Toberer, A. Saramat, K. Kurosaki, A. Charoenphakdee, S. Yamanaka, and G. J. Snyder, Science **321**, 554 (2008).

[5] A. Zevalkink, S. Chanakian, U. Aydemir, A. Ormeci, G. Pomrehn, S. Bux, J. P. Fleurial, and G. J. Snyder, J. Phys.: Condens. Matter **27**, 015801 (2015).

[6] S. Guo, K. Yang, Z. Zeng, and Y. Zhang, Phys. Chem. Chem. Phys. **20**, 14441 (2018).

[7] Y. Zhang, E. Skoug, J. Cain, V. Ozoliņš, D. Morelli, and C. Wolverton, Phys. Rev. B **85**, 054306 (2012).

[8] Y. Zhang, V. Ozoliņš, D. Morelli, and C. Wolverton, Chem. Mater. **26**, 3427 (2014).

[9] Y. Fu, D. J. Singh, W. Li, and L. Zhang, Phys. Rev. B **94**, 075122 (2016).

[10] T. Jia, G. Chen, and Y. Zhang, Phys. Rev. B **95**, 155206 (2017).

[11] Y. Fu, X. He, L. Zhang, and D. J. Singh, Phys. Rev. B **97**, 024301 (2018).

[12] Z. Feng, T. Jia, J. Zhang, Y. Wang, and Y. Zhang, Phys. Rev. B **96**, 235205 (2017).

[13] H. Goldsmid, *Thermoelectric refrigeration* (Springer, New York, 2013).

[14] R. P. Chasmar and R. Stratton, J. Electron. Control **7**, 52 (1959).

[15] Y. Pei, H. Wang, and G. J. Snyder, Adv. Mater. **24**, 6125 (2012).

[16] A. Banik, U. S. Shenoy, S. Anand, U. V. Waghmare, and K. Biswas, Chem. Mater. **27**, 581 (2015).

[17] Z. Feng, J. Zhang, Y. Yan, G. Zhang, C. Wang, C. Peng, F. Ren, Y. Wang, and Z. Cheng, Sci. Rep. **7**, 2572 (2017).

[18] X. Liu, L. Xi, W. Qiu, J. Yang, T. Zhu, X. Zhao, and W. Zhang, Adv. Electron. Mater. **2**, 1500284 (2016).

[19] S. R. Brown, S. M. Kauzlarich, F. Gascoin, and G. J. Snyder, Chem. Mater. **18**, 1873 (2006).

[20] Y. Tang, R. Hanus, S.-w. Chen, and G. J. Snyder, Nat. Commun. **6**, 7584 (2015).

[21] W. Yim and F. Rosi, Solid-State Electronics **15**, 1121 (1972).

[22] B. Poudel, Q. Hao, Y. Ma, Y. Lan, A. Minnich, B. Yu, X. Yan, D. Wang, A. Muto, D. Vashaee, X. Chen, J. Liu, M. S. Dresselhaus, G. Chen, and Z. Ren, Science **320**, 634 (2008).

[23] D. S. Parker, A. F. May, and D. J. Singh, Phys. Rev. Appl. **3**, 064003 (2015).

[24] S. N. Guin, V. Srihari, and K. Biswas, J. Mater. Chem. A **3**, 648 (2015).

[25] X. Liu, D. Jin, and X. Liang, Appl. Phys. Lett. **109**, 133901 (2016).

[26] V. Rajaji, P. S. Malavi, S. S. R. K. C. Yamijala, Y. A. Sorb, U. Dutta, S. N. Guin, B. Joseph, S. K. Pati, S. Karmakar, K. Biswas, and C. Narayana, Appl. Phys. Lett. **109**, 171903 (2016).

[27] Y. Goto, A. Nishida, H. Nishiate, M. Murata, C. H. Lee, A. Miura, C. Moriyoshi, Y. Kuroiwa, and Y. Mizuguchi, Dalton trans. **47**, 2575 (2018).

[28] Y. Guan, Y. Huang, D. Wu, D. Feng, M. He, and J. He, Appl. Phys. Lett. **112**, 213905 (2018).

[29] M. Zou, Q. Liu, C.-F. Wu, T.-R. Wei, Q. Tan, J.-F. Li, and F. Chen, RSC Advances **8**, 7055 (2018).

[30] C. Xiao, X. Qin, J. Zhang, R. An, J. Xu, K. Li, B. Cao, J. Yang, B. Ye, and Y. Xie, J. Am. Chem. Soc. **134**, 18460 (2012).

[31] C. Xiao, J. Xu, B. Cao, K. Li, M. Kong, and Y. Xie, J. Am. Chem. Soc. **134**, 7971 (2012).

[32] L. Pan, D. Berardan, and N. Dragoe, J. Am. Chem. Soc. **135**, 4914 (2013).

[33] P. E. Blöchl, Phys. Rev. B **50**, 17953 (1994).

[34] G. Kresse and J. Furthmüller, Phys. Rev. B **54**, 11169 (1996).

[35] J. P. Perdew, K. Burke, and M. Ernzerhof, Phys. Rev. Lett. **77**, 3865 (1996).

[36] F. Tran and P. Blaha, Phys. Rev. Lett. **102**, 226401 (2009).

[37] D. J. Singh and L. Nordstrom, *Planewaves, Pseudopotentials, and the LAPW Method* (Springer Science & Business Media, Dordrecht, London, 2006).

[38] P. Hohenberg and W. Kohn, Phys. Rev. **136**, B864 (1964).

[39] P. Blaha, K. Schwarz, G. Madsen, D. Kvasnicka, and J. Luitz, *An Augmented Plane Wave Plus Local Orbital Program for Calculating Crystal Properties* (Vienna University of Technology, Vienna, Austria, 2001).

[40] J. M. Ziman, *Electrons and Phonons: the Theory of Transport Phenomena in Solids* (Oxford University Press, Oxford, New York, 1960).

[41] G. K. H. Madsen, K. Schwarz, P. Blaha, and D. J. Singh, Phys. Rev. B **68**, 125212 (2003).

[42] G. K. H. Madsen and D. J. Singh, Comput. Phys. Commun. **175**, 67 (2006).

[43] V. Popescu and A. Zunger, Phys. Rev. B **85**, 085201 (2012).

[44] W. Yin, S. Wei, M. M. Al-Jassim, J. Turner, and Y. Yan, Phys. Rev. B **83**, 155102 (2011).

[45] H. Dixit, N. Tandon, S. Cottenier, R. Saniz, D. Lamoen, and B. Partoens, Phys. Rev. B **87**, 174101 (2013).

[46] S. Lany and A. Zunger, Phys. Rev. B **78**, 235104 (2008).

[47] F. Bocher, S. P. Culver, J. Peilstocker, K. S. Weldert, and W. G. Zeier, Dalton trans. **46**, 3906 (2017).

[48] See Supplemental Material at http://link.aps.org/supplemental/ for the isoenergy surface of the conduction bands for $AgBiSe_2$, the band structures of pristine $AgBiSe_2$ and Ag vacancy system, the electron relaxation times from the experimental fitting and the deformation potential approach at 300 K, the thermoelectric properties of $AgBiSe_2$ and the available experimental data for comparison, the formation energies of Cu, Ru, Rh, Pd impurities at three different conditions, the band structures for pristine, and Cu/Rh/Rh/Pd-doped system within two different supercell.

[49] D. Parker, X. Chen, and D. J. Singh, Phys. Rev. Lett. **110**, 146601 (2013).

[50] H. Shi, W. Ming, D. S. Parker, M.-H. Du, and D. J. Singh, Phys. Rev. B **95**, 195207 (2017).

[51] G. Xing, J. Sun, Y. Li, X. Fan, W. Zheng, and D. J. Singh, Phys. Rev. Mater. **1**, 065405 (2017).

[52] D. Parker and D. J. Singh, Phys. Rev. B **82**, 035204 (2010).

[53] W. E. Pickett, J. Supercond. **4**, 397 (1991).

[54] K. P. Ong, D. J. Singh, and P. Wu, Phys. Rev. B **83**, 115110 (2011).

[55] R. Guo, X. Wang, Y. Kuang, and B. Huang, Phys. Rev. B **92**, 115202 (2015).

[56] A. F. May, E. S. Toberer, A. Saramat, and G. J. Snyder, Phys. Rev. B **80**, 125205 (2009).

[57] Z. Liu, Y. Wang, J. Mao, H. Geng, J. Shuai, Y. Wang, R. He, W. Cai, J. Sui, and Z. Ren, Adv. Energy Mater. **6**, 1502269 (2016).

[58] S. Lin, W. Li, Z. Chen, J. Shen, B. Ge, and Y. Pei, Nat. Commun. **7**, 10287 (2016).

[59] G. J. Snyder and E. S. Toberer, Nat. Mater. **7**, 105 (2008).

[60] Z. Feng, Y. Wang, Y. Yan, G. Zhang, J. Yang, J. Zhang, and C. Wang, Phys. Chem. Chem. Phys. **17**, 15156 (2015).

[61] J. P. Heremans, B. Wiendlocha, and A. M. Chamoire, Energy Environ. Sci. **5**, 5510 (2012).

Table I. Chemical potentials at the A, B, C, D and E points labeled in Fig. 1 (unit: eV).

Point	$\Delta\mu_{Ag}$	$\Delta\mu_{Bi}$	$\Delta\mu_{Se}$
A	0	-0.68	-0.21
C	0	-0.12	-0.49
B	-0.11	-0.99	0
D	-0.20	-0.90	0
E	-0.20	-0.48	-0.21

Table II. Relevant atomic energy levels of *s*, *p*, and *d* states of different atoms (Ag, Bi, Se, Cu, Ru, Rh and Pd). (unit: eV)

Atom	Valence state	*s*-state	*p*-state	*d*-state
Ag	$4d^{10}5s^{1}$	-4.47		-7.44
Bi	$6s^{2}6p^{2}$	-14.23	-4.29	
Se	$4s^{2}4p^{4}$	-17.14	-6.35	
Cu	$3d^{10}4s^{1}$	-4.57		-4.94
Ru	$4d^{7}5s^{1}$	-0.55		-3.46
Rh	$4d^{8}5s^{1}$	-0.44		-3.40
Pd	$4d^{10}$			-4.41

Table III. The chemical potentials of Cu, Ru, Rh, and Pd in the doped system under different conditions (unit: eV).

	A (0, -0.68 eV, -0.21 eV)	B (-0.11 eV, -0.99 eV, 0)	C (0, -0.12 eV, -0.49 eV)
Cu	-0.99	-0.23	0
Ru	-0.79	-1.21	-0.23
Rh	-0.82	-1.38	-0.16
Pd	-0.44	-0.79	-0.21

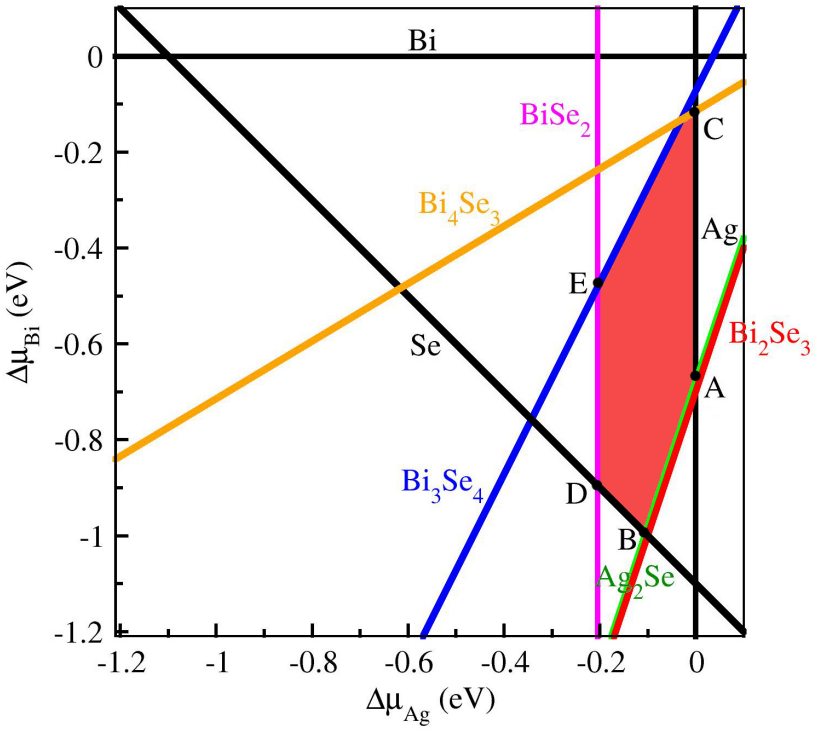

Fig. 1. (Color online) Accessible range of chemical potential (red shaded region) for the equilibrium growth conditions of the hexagonal $AgBiSe_2$ phase. The specific points are chosen for the representative chemical potentials to be used for the defect formation energy calculations.

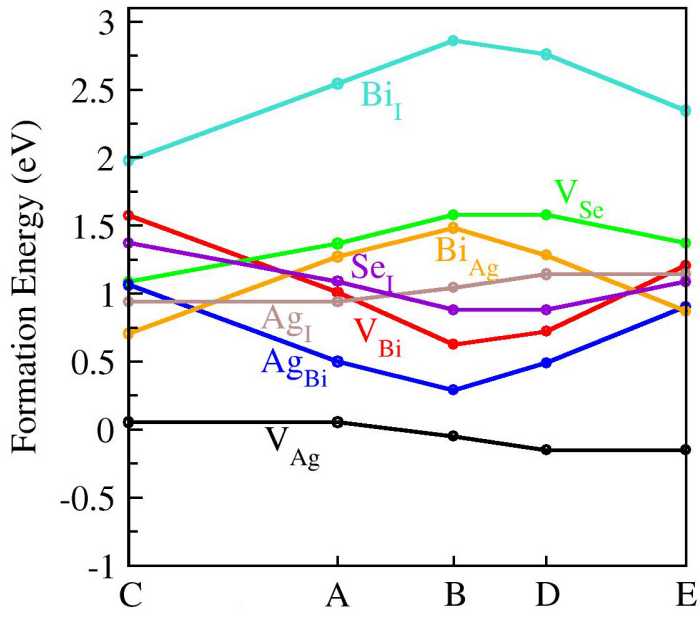

Fig. 2. (Color online) Formation energies of neutral defects in $AgBiSe_2$ as a function of the chemical potential at points A-E shown in Fig. 1 and Table I.

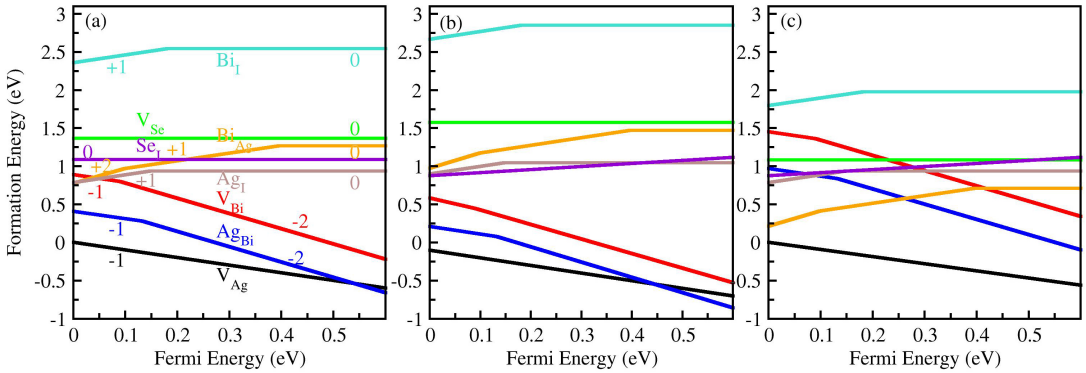

Fig. 3. (Color online) Theoretically calculated formation energies of intrinsic charged point defects in $AgBiSe_2$ as a function of the Fermi level, with chemical potentials under the (a) Ag-rich [point-A (0, -0.68 eV, -0.21 eV) in Fig. 1], (b) Se-rich [point-B (-0.11 eV, -0.99 eV, 0) in Fig. 1], and (c) Ag-rich/more Se-poor [point-C (0, -0.12 eV, -0.49 eV) in Fig. 1] conditions.

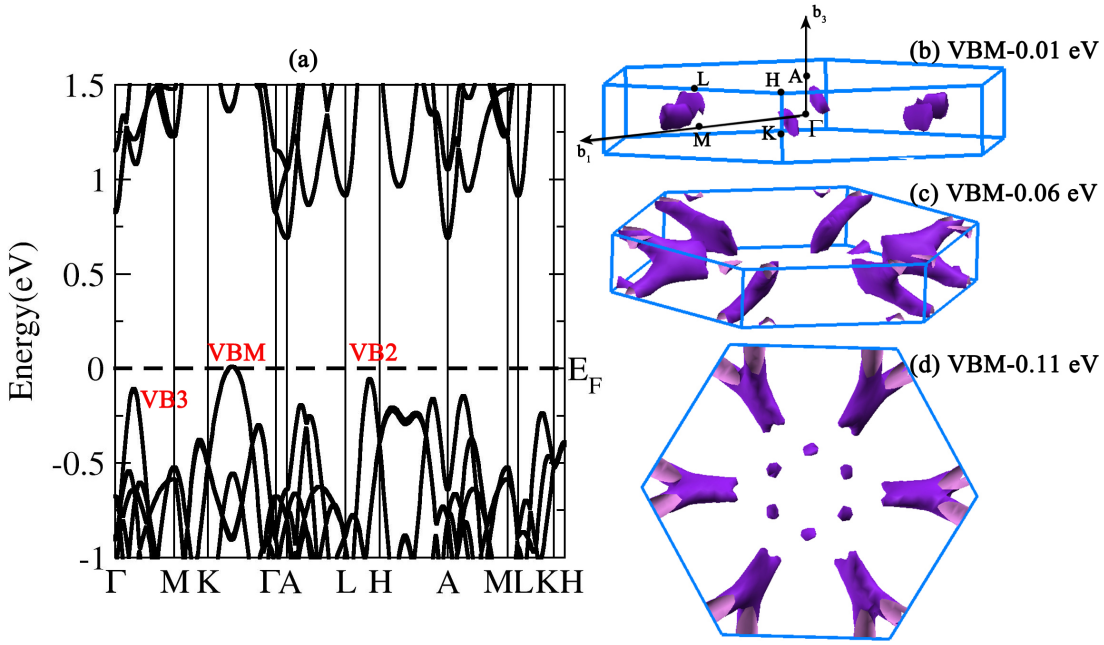

Fig. 4. (a) (Color online) (a) Calculated band structure of the pristine $AgBiSe_2$ along high symmetry points in BZ. The black dashed line represents the Fermi level. The calculated isoenergy surfaces for $AgBiSe_2$ near the VBM are shown at (b) VBM-0.01 eV, (c) VBM-0.06 eV, (d) VBM-0.11 eV.

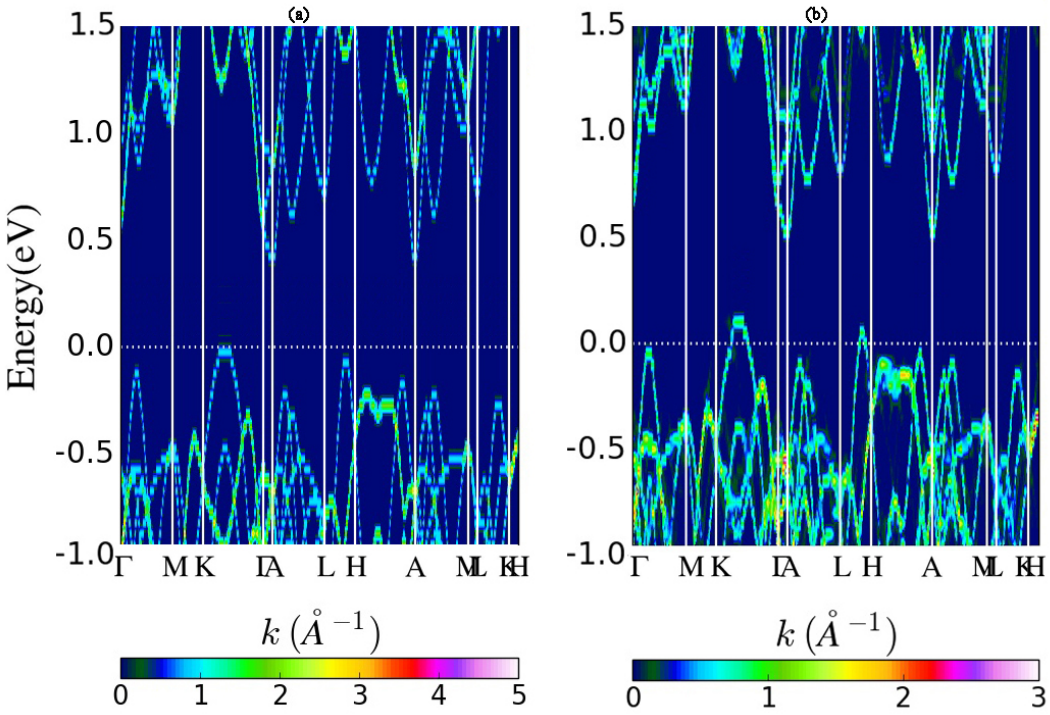

Fig. 5. (Color online) The band structures of (a) pristine $AgBiSe_2$ (b) Ag vacancy after band unfolding.

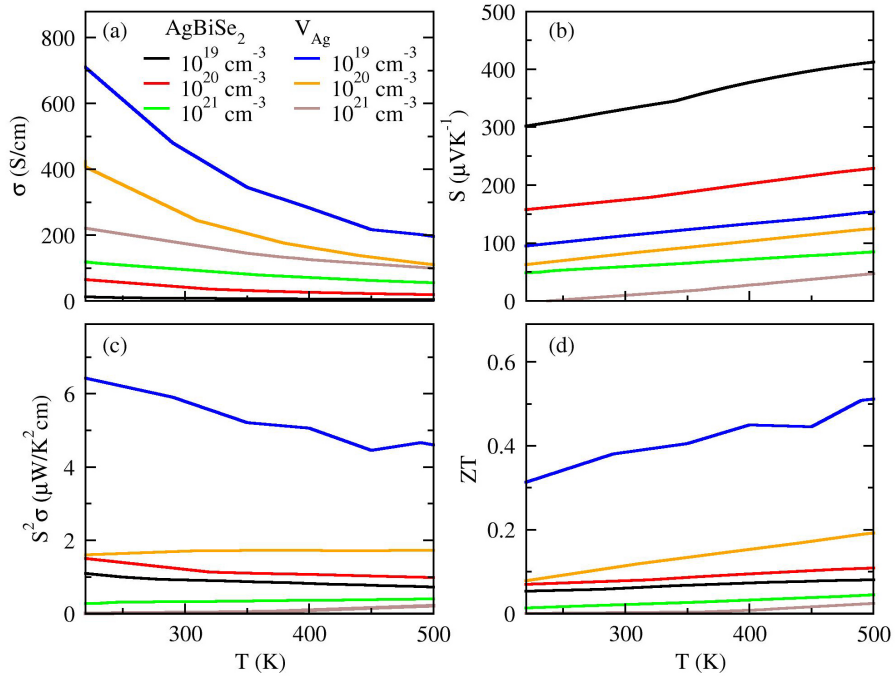

Fig. 6. Theoretically calculated thermoelectric properties (σ, S, $S^2σ$, and ZT) of $AgBiSe_2$ and Ag vacancy defect system as a function of temperature and concentrations.

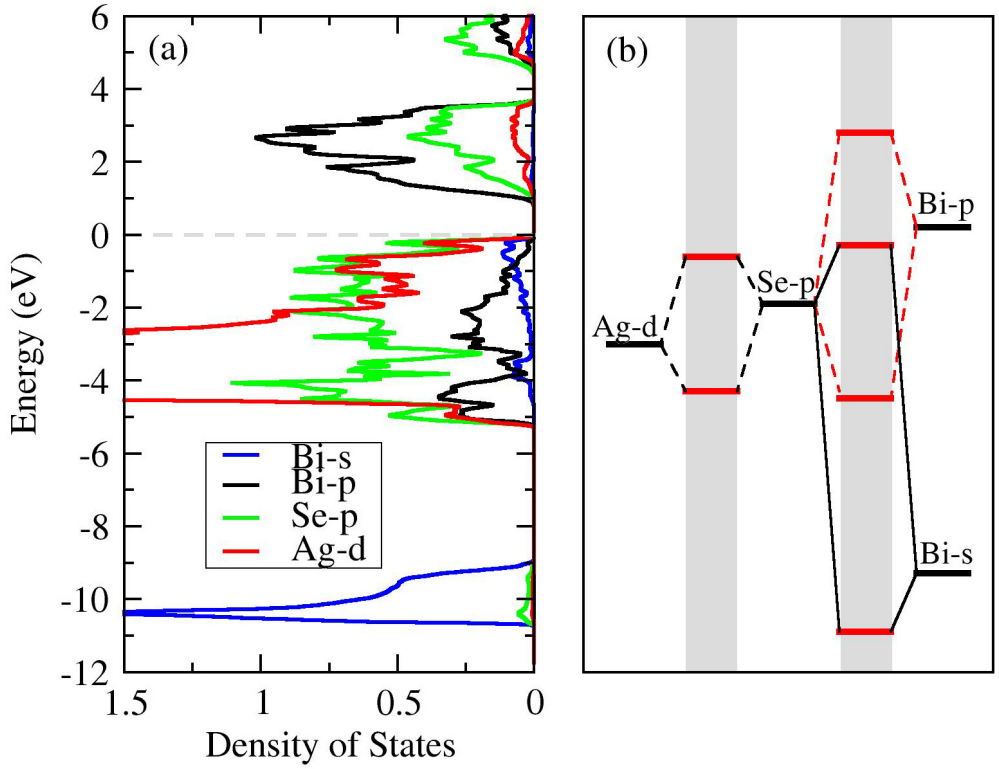

Fig. 7. (Color online) (a) Projected density of states of $AgBiSe_2$. (b) Schematic of interatomic interactions between the main valence states for energy-band formation, where the bonding and antibonding states are formed in the shaded region. The position of energy levels in the shaded region of (b) corresponds to states in (a). The Ag-*d* atomic level sits at its *d*-band center (~-3.0 eV) and other atomic orbital levels are positioned relative to Ag-*d*. In $AgBiSe_2$, the Ag d-band are narrow and occupied which facilitated the analysis, and we estimate the d-band center by averaging the valence d-band DOS.

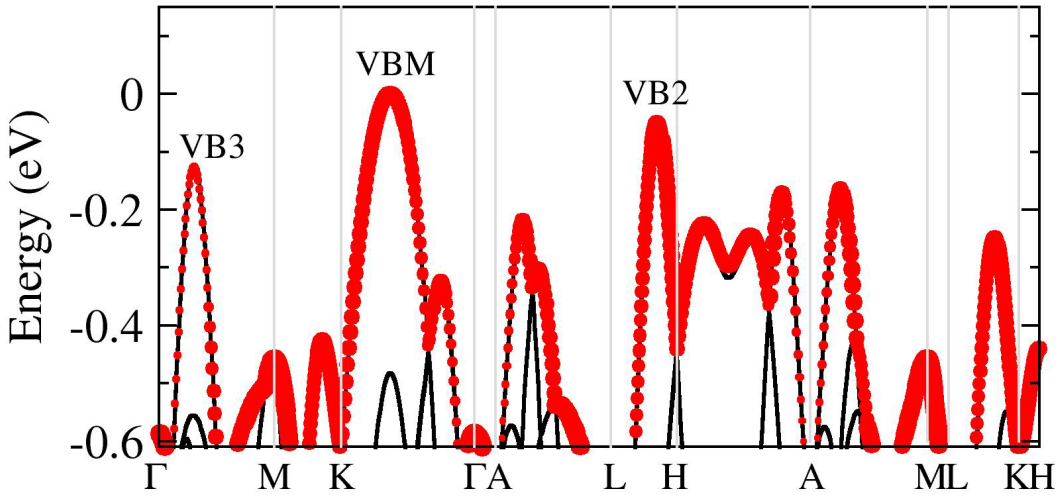

Fig. 8. (Color online) Projection of the $AgBiSe_2$ band wave functions onto the Ag-d orbitals (the big red dots).